LETTER

Colouration by total internal reflection and interference at microscale concave interfaces

Amy E. Goodling[1,6], Sara Nagelberg[2,6], Bryan Kaehr[3], Caleb H. Meredith[1], Seong Ik Cheon[4], Ashley P. Saunders[4], Mathias Kolle[2] & Lauren D. Zarzar[4,5]*

Many physical phenomena create colour: spectrally selective light absorption by pigments and dyes[1,2], material-specific optical dispersion[3] and light interference[4–11] in micrometre-scale and nanometre-scale periodic structures[12–17]. In addition, scattering, diffraction and interference mechanisms are inherent to spherical droplets[18], which contribute to atmospheric phenomena such as glories, coronas and rainbows[19]. Here we describe a previously unrecognized mechanism for creating iridescent structural colour with large angular spectral separation. Light travelling along different trajectories of total internal reflection at a concave optical interface can interfere to generate brilliant patterns of colour. The effect is generated at interfaces with dimensions that are orders of magnitude larger than the wavelength of visible light and is readily observed in systems as simple as water drops condensed on a transparent substrate. We also exploit this phenomenon in complex systems, including multiphase droplets, three-dimensional patterned polymer surfaces and solid microparticles, to create patterns of iridescent colour that are consistent with theoretical predictions. Such controllable structural colouration is straightforward to generate at microscale interfaces, so we expect that the design principles and predictive theory outlined here will be of interest both for fundamental exploration in optics and for application in functional colloidal inks and paints, displays and sensors.

We observed the structural colouration within monodisperse, biphasic Janus oil droplets containing heptane (refractive index $n_H \approx 1.37$) and perfluorohexane ($n_F \approx 1.27$) dispersed in aqueous surfactant (Fig. 1a; see Methods for determination of refractive indices). Upon illumination with collimated white light from above, droplets with an upward-facing concave internal interface between the constituent oils exhibit intense angle-dependent colouration in reflection (Fig. 1b; Supplementary Video 1). Microscopic observations reveal that the reflected light emanates from a ring near the droplets' three-phase contact line (Fig. 1c), suggesting that the colour is due to light–matter interactions within single droplets rather than periodic droplet arrangement. Polydisperse droplets of identical oil volume ratios and contact angles were found to exhibit size-dependent colour (Fig. 1d); the resulting mix of colours gives rise to a glittery white appearance as seen by the unaided eye (Fig. 1e). Droplets polymerized into solid particles retain reflected colour but do not orient with gravity as well as the liquid droplets, highlighting the importance of the orientation of the hydrocarbon–fluorocarbon interface with respect to the light in generating the optical effect (Fig. 1f). Given that the orientation of the droplet-internal interface was essential to the optical mechanism, we wondered whether the colours could be replicated in simpler materials with a similar concave geometry, such as that of a sessile droplet. Upon condensing water onto the underside of a transparent, polystyrene Petri dish lid (advancing contact angle, 70°), we observed substantial colour separation and iridescence (Fig. 1g; Supplementary Video 2). Again, the coloured light emanates from near the solid–liquid contact line and the effect is dependent on

sessile-droplet diameter and contact angle (Fig. 1h, i). Solid polymeric hemispheres of dimensions comparable to those of the sessile droplets also show similar behaviour (Extended Data Fig. 1) and display varying reflected colour when exposed to media of different refractive index (Supplementary Video 3). As a way of systematically quantifying the light scattering and iridescence of these materials and capturing the entire angular colour distribution, we projected the reflected light onto a translucent hemispherical screen (half of a ping-pong ball). This technique allows us to visualize all of the colours for all viewing angles in a single image (Fig. 2a–c). We observed that the angular separation of the colours is large, approximately 30–35° from red to blue, for the systems described in Fig. 1. This colour separation cannot be explained with known structural colouration mechanisms, which are incompatible with the large length scales and geometries of these interfaces. We were thereby motivated to discover the origin of this iridescence.

Given that the colour separation phenomenon is generalizable to microscale concave interfaces with adjacent volumes of high- and low-refractive-index media, and that the light reflects from near the edge of the concave interface, we hypothesized that total internal reflection (TIR) of light along the concave interface has an important role. However, although TIR explains how light is reflected with pronounced intensity, it alone cannot account for the colour variations observed. Material dispersion can also not accurately describe the angular colour separation nor the size dependence in a simple ray-tracing model (Extended Data Fig. 2). Consequently, another optical mechanism must be at play. In general, iridescent structural colours are caused by interference of light waves taking different paths through a material[20]. In photonic crystals or gratings, such interference is created through surface or volume periodicity of the order of the wavelength of light, which is not present in our system. Interference of light within spherical water droplets is responsible for the colourful atmospheric effect known as a glory. Typically, optical phenomena caused by scattering spheres, such as glories and rainbows, are modelled using Mie scattering theory[19]. However, Mie theory applies only to particles with spherical symmetry, which is not present in the systems we consider[21]; the sessile droplets and domes are spherical caps and the concave interior interfaces of the biphasic droplets similarly break spherical symmetry. This broken symmetry enables TIR of light along a concave interface, which is not possible in perfect spheres. Hence, we hypothesized that the observed colours result from the interference of this light propagating by TIR on different paths along a concave interface.

To test our prediction, we first considered a simplified system in which light would be expected to propagate in a single plane, such as in a cylindrical segment. Provided the incident light direction is perpendicular to the cylinder symmetry axis, the reflected rays are expected to all lie within the plane perpendicular to that axis (Fig. 3a). We used multiphoton lithography to print arrays of cylindrical (Fig. 3b, c) and polygonal segments of varying numbers of sides (Extended Data Fig. 3) and observed reflected iridescent colour for all structures that supported multiple trajectories of TIR. The interference of light in the
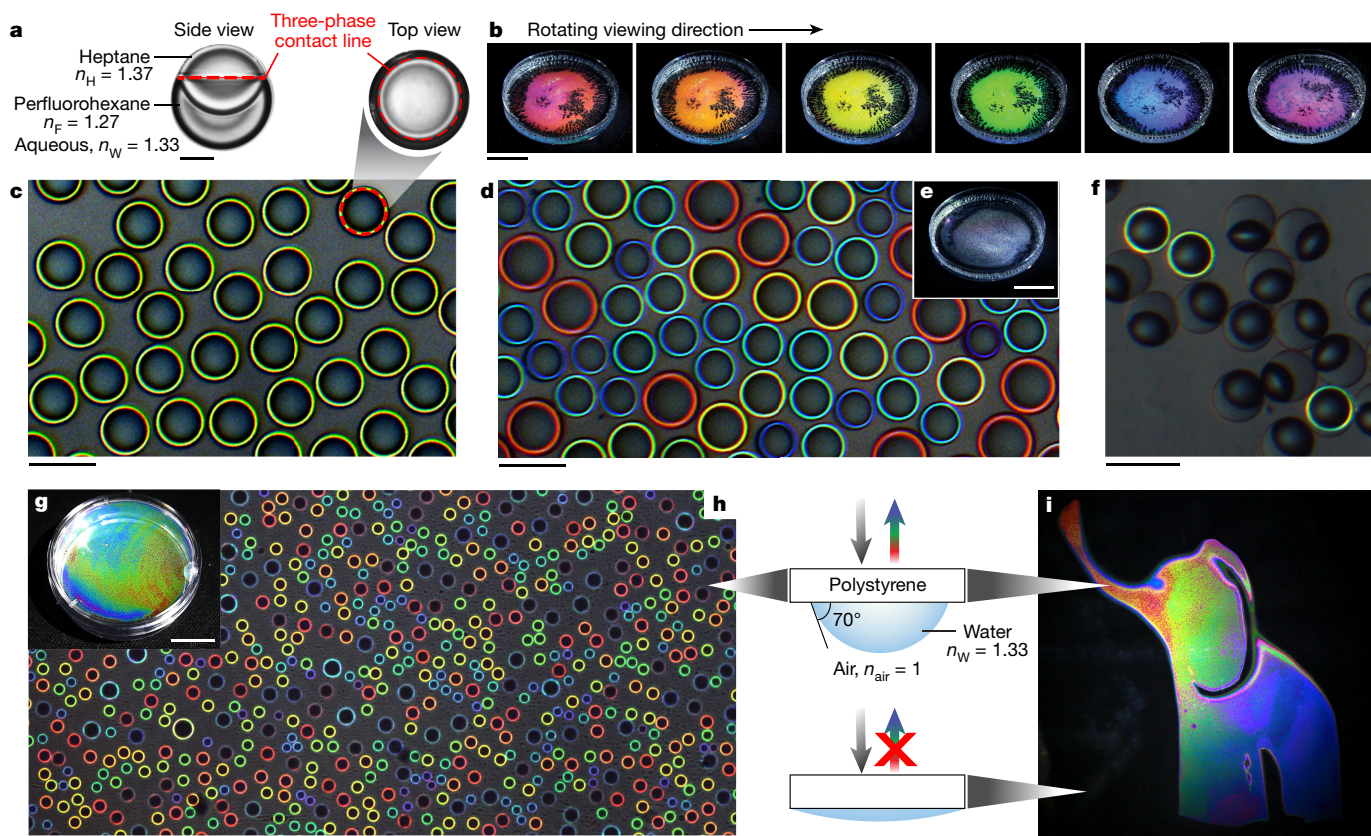
Fig. 1 | Microscale concave surfaces display colourful iridescence in reflection. a, Schematic and optical micrograph showing the biphasic droplet geometry and composition used in **b–e**. The droplets orient with gravity with the denser perfluorohexane side downward, as shown. Scale bar, 25 μm. **b**, A Petri dish containing a monolayer of monodisperse droplets as shown in **a** was illuminated with collimated white light from a fixed direction and photographed at several different observation angles to demonstrate variation in reflected colour (Supplementary Video 1). Scale bar, 2 cm. **c**, Microscopically, each droplet from **b** reflects the same colour, irrespective of the location of neighbouring drops. The colour always emanates from near the three-phase contact line of the droplets. Scale bar, 100 μm. **d**, Polydisperse droplets all having the same morphology and composition as in **a** but varying size show different colours in reflection. Scale bar, 100 μm. **e**, Macroscopically, the polydisperse droplets in **d** reflect glittery white light. Scale bar, 2 cm. **f**, Reflection optical micrograph of solid particles dispersed in water of the same general morphology as shown in **a**. Trimethyloylpropane triacrylate ($n \approx 1.56$) was used instead of heptane, Sartomer fluorinated oligomer ($n \approx 1.33$) mixed with 1H,1H,2H,2H-perfluorodecyl acrylate ($n \approx 1.34$) replaced

perfluorohexane, and the monomers were polymerized by ultraviolet initiation (see Methods). The particles did not orient as uniformly as did the liquid droplets, highlighting the importance of the orientation of the hydrocarbon–fluorocarbon interface in enabling reflection. Scale bar, 100 μm. **g**, Photograph of water droplets condensed onto the underside of a polystyrene Petri dish lid illuminated with white light and viewed in reflection (Supplementary Video 2). Scale bar, 1 cm. **h**, Reflectance optical micrograph of water droplets condensed onto a polystyrene Petri dish showing how the colour emanates from near the contact line and varies with droplet diameter. Scale bar, 200 μm. **i**, Reflectance photograph showing the colourful image created when water is condensed onto a polystyrene Petri dish with surface hydrophilicity patterned in the shape of an elephant. Although there is water condensed over the entire surface, the more hydrophilic ultraviolet-ozone treated regions appear black while the untreated regions (contact angle, 70°) reflect colour, demonstrating the importance of the contact angle in generating the optical effect. Scale bar, 3 cm. The inset diagram depicts how the contact angle of the droplets on surfaces shown in **i** and **h** influence the reflected iridescence.

cylindrical segments can be theoretically modelled by considering all the different paths that light can take along the interface and accounting for the total phase accumulated along each trajectory (Fig. 3d). Thus, we can determine the intensity I as a function of wavelength for each light incidence direction and observation angle (Fig. 3e). Analytically, this can be expressed as the sum of the complex amplitudes of all light paths that are possible for a given angle of light incidence (θ_{in}) and a fixed observation direction (θ_{out}):

$$I = \left| \sum_{\substack{m \\ \text{all possible paths}}} A_m(\alpha_m) \left[r_m\left(\alpha_m, \frac{n_1}{n_2}\right) \right]^m \exp\left(\frac{2\pi i n_1}{\lambda_0} l_m(\alpha_m) \right) \right|^2 \quad (1)$$

where the index of summation m represents the number of reflections that occur for each trajectory. In the example in Fig. 3d, this would be the sum over the three different paths shown, so that m runs from 2 to 4. The local angle of incidence is

$$\alpha_m = \frac{\pi}{2} - \frac{\pi - \theta_{in} + \theta_{out}}{2m} \quad (2)$$

A_m is an amplitude factor, r_m is the complex Fresnel reflection coefficient (which effects a phase shift upon each reflection), n_1 and n_2 are the refractive indices of the medium above and below the interface respectively, and λ_0 is the wavelength of light in air. The phase change due to propagation is captured in the exponential where $l_m = 2mR\cos(\alpha_m)$ is the physical path length of each trajectory, with R being the optical interface's radius of curvature. We note that the intensity I is a function of the incident light's wavelength λ_0, the incidence angle θ_{in} and the observation angle θ_{out}. For the detailed derivation, see Supplementary Discussion section 'Full derivation of the analytical description of the interference phenomenon in 2D'. From the analytically obtained spectral information, we predicted the colours that should be observed (see Supplementary Discussion section 'Converting spectra into colors') and they matched well with the experimentally determined angular colour distribution (Fig. 3f, g; see Supplementary
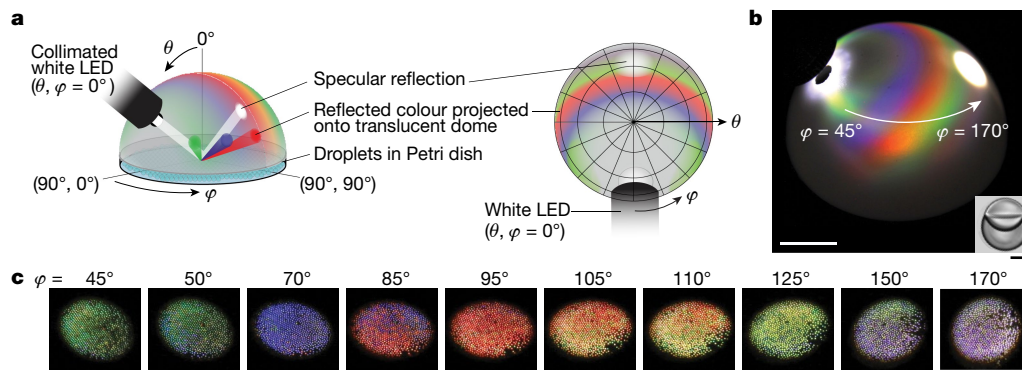
Fig. 2 | Biphasic droplet iridescence mapped in three dimensions.
a, Side and top view schematics of the experimental setup and coordinate system used to visualize the iridescent colour reflected from the droplets in three dimensions. A translucent hemispherical dome screen (half a ping-pong ball) was placed over a Petri dish containing monodisperse droplets. Collimated white light from a light-emitting diode (LED) was introduced through a 3-mm hole cut into the side of the domed screen. Colours reflected from the drops projected onto the internal surface of the dome screen. **b**, Side view photograph of an exemplary iridescence pattern (scale bar, 1 cm) with illumination at $\theta = 40°$ and an inset showing the shape of droplets used (scale bar, 50 μm). **c**, The screen from **b** was removed and the droplets were photographed at different viewing angles φ under the same illumination angle to demonstrate correlation of the macroscopic colours with the mapped angular position of colour onto the screen in **b**. Scale bar, 2 mm.

Discussion section 'Quantitative angle measurements from the experimentally determined angular color distributions').

We next aimed to predict the scattering behaviour of three-dimensional structures. The two-dimensional model was readily extended to treat three-dimensional spherical caps by recognizing that all reflections occur within the plane containing the incoming ray of light and the centre of curvature of the spherical interface (Fig. 4a). In this plane, we denote the effective light incidence and reflection angles, measured from the spherical cap's in-plane surface normal, as β_{in} and β_{out}. η_{eff} is the effective opening angle. A full derivation of the angles within this plane, in relation to the global coordinates θ_{in}, θ_{out}, φ_{out} and η as shown in Fig. 4a, is given in the Supplementary Discussion section 'Extension of the theoretical description to 3D spherical concave optical interfaces'. To compare results from the model with experiment, we used the biphasic heptane–perfluorohexane droplets but index-matched the aqueous phase to the heptane phase, allowing us to disregard refraction at the droplets' curved upper interface. We found very good agreement between the model and experiment (Fig. 4b–h).

We used this three-dimensional model to better understand how various geometrical and material-specific parameters affect the colour distribution. The total phase change for a given path, and thus the interference condition, depends on the product $n_1 R$ in the optical path
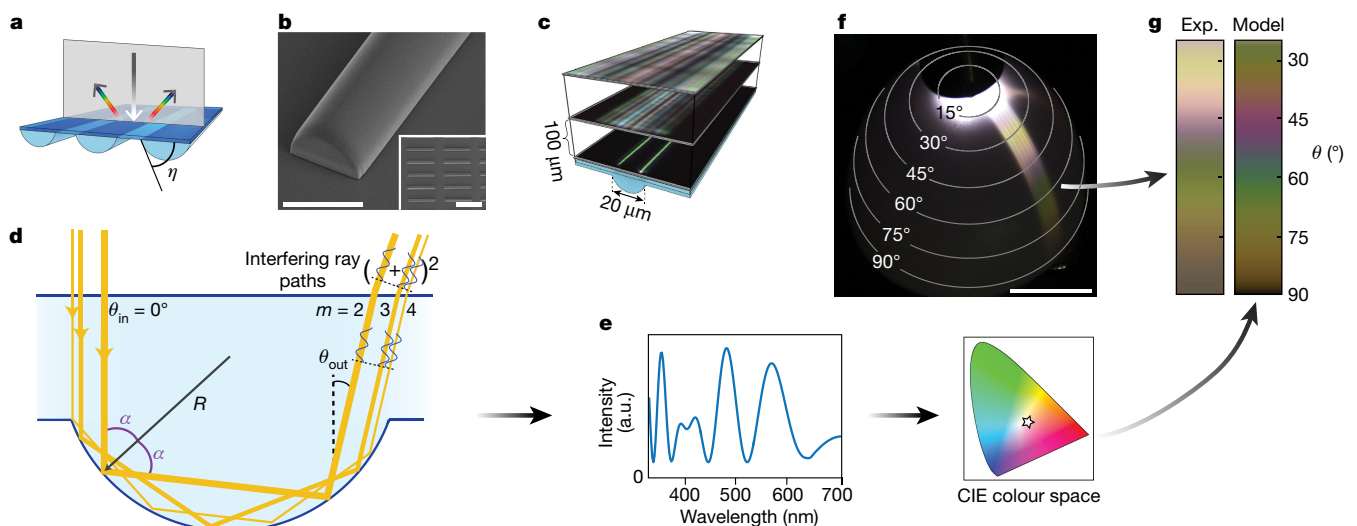

Fig. 3 | Two-dimensional model of the optical mechanism for structural colour generation upon cascading total internal reflections. **a**, Diagram of horizontal cylindrical segments with η, the contact angle, defined. **b**, Scanning electron micrographs of the horizontal cylindrical segments as fabricated by multiphoton lithography with a radius of curvature of 10.64 μm and a contact angle of 70°. The higher-magnification image shows the cylindrical edge (scale bar, 20 μm) and the lower-magnification inset shows a portion of the structure array (scale bar, 200 μm). **c**, Optical micrographs of a cylindrical segment, in focus and defocused by 100 μm and 200 μm, showing how the reflected colour patterns evolve farther from the surface. **d**, Diagram of three rays taking different trajectories along the concave interface that interfere, causing the observed colouration. The input and output angles (θ_{in}, θ_{out}) are measured from the global sample surface normal to the left (θ_{out} is negative as shown). **e**, Spectrum derived from equation (1) for $(\theta_{in}, \theta_{out}) = (0°, -13.09°)$ (corresponding to 0° input, −20° output in air). The image below shows the coordinates of this spectrum in the CIE (International Commission on Illumination/Commission Internationale de l'Éclairage) colour space. **f**, Reflected colour distribution from the horizontal cylindrical segments when illuminated at normal incidence. Lines of constant θ are shown. Scale bar, 2 cm. **g**, Comparison of colour distribution from model and experiment (Exp.) for 0° illumination of the 70° contact angle horizontal cylindrical segments. The input illumination of the calculated colours was averaged over a cone from −5° to +5° in order to approximate the divergence of the light source, and the lamp's spectrum was used for input spectral intensities in the model. The brightness of the experimental dataset was increased by multiplying by a factor of $(1 - 0.8\cos\theta)$ in order to better see the colours at high angles. Low angles were obscured by the specular reflection.
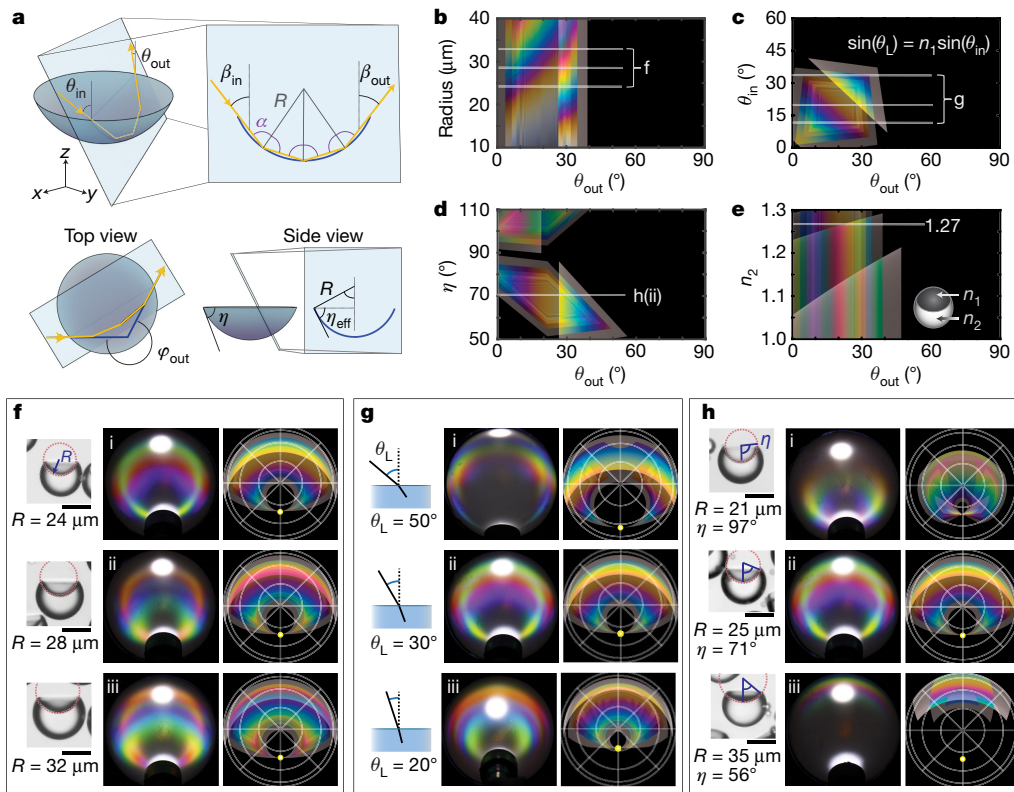
Fig. 4 | Extension of model to three-dimensional spherical interfaces and comparison with experiment for index-matched Janus droplets. a, Diagram of a light path in a three-dimensional spherical cap. Light is confined to the plane through the centre of curvature of the interface and the line defined by the incoming light ray direction. Within this plane, the system can be reduced to two dimensions with effective opening angle, η_{eff}, and effective input and output angles, β_{in} and β_{out}. **b–e**, The colour distribution as a function of θ_{out} when changing: **b**, the radius of curvature, **c**, the illumination direction within the medium with refractive index n_1, **d**, the opening angle η, and **e**, the refractive index of the fluorocarbon phase, n_2. The default parameters used were $R = 25\,\mu m$,

$\eta = 71°$, $\theta_{in} = 21.4°$, $n_1 = 1.37$ and $n_2 = 1.27$, and one parameter at a time was varied. These results for θ_{in} and θ_{out} in the index-matched medium are related to the measured angles by Snell's law. **f–h**, Comparison of experimental iridescence maps of index-matched Janus droplets with the predicted three-dimensional calculation for various sizes (**f**), illumination angles (**g**) and droplet morphologies (**h**). **f**, Effect of size (radius of curvature) where the contact angle and illumination were fixed at $\eta = 71°$ and $\theta_L = 30°$ respectively. **g**, Effect of illumination angle (using the same droplet sample as in **h(ii)**). **h**, Effect of droplet morphology ($\theta_L = 30°$). Scale bars in **f** and **h**, 50 μm.

length and the refractive index contrast in the Fresnel coefficient $r_m\left(\alpha_m, \frac{n_1}{n_2}\right)$. The allowed trajectories for a given $(\theta_{in}, \theta_{out})$ are set by the opening angle η as well as illumination and observation directions. Figure 4b–e shows how each of these parameters (R, θ_{in}, η and n_2) affects the colours observed as a function of observation direction θ_{out} for the azimuthal angle $\varphi_{out} = 180°$. As the radius of curvature R increases, the colour patterns shift to larger angles and the spread of colours decreases, as shown in Fig. 4b, f and Extended Data Fig. 4a).

The angular location of the colour bands varies almost linearly with the illumination direction θ_{in}, as seen in Fig. 4c, g and Extended Data Fig. 4b. This can be understood by interpreting a change in illumination angle θ_{in} as a rotation of all ray paths around the centre of curvature of the interface. Once rotated too far, a ray trajectory may no longer be available, which is evident in the sharp changes in colour in Fig. 4c. The opening angle η does not affect the phase of the light; consequently, the locations of the colour bands are constant as η is varied (Fig. 4d).
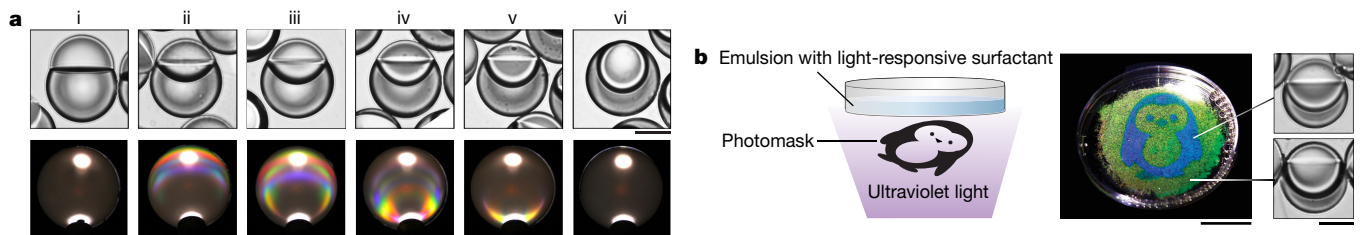

Fig. 5 | Iridescence of biphasic oil droplets depends on the curvature of the oil–oil interface. a, Alteration of the internal interfacial curvature in heptane–perfluorohexane biphasic droplets (similar to those shown in Fig. 1a) caused a corresponding change in the iridescence. Biphasic droplets with a flat internal interface (far left) and a fully enclosed spherical internal interface (far right) did not display any reflected colour. The top row shows optical micrographs of example droplets. Scale bar, 50 μm. The bottom row shows photographs of the iridescence pattern as

viewed from $\theta = 0°$ with an illumination angle of $\theta = 35°$. Scale bar, 1 cm. **b**, A light-responsive surfactant was added to allow photo-patterning of the emulsion shape, and hence, reflected colour. Shown is a photograph of a penguin image (Shutterstock, https://www.shutterstock.com/image-vector/simple-card-illustration-cartoon-penguin-65675242) patterned in droplets in a Petri dish (scale bar, 2 cm) and side view images of the droplet shapes giving rise to the blue and green colours (scale bar, 50 μm).

However, whether a specific trajectory is possible strongly depends on η. Regions of grey indicate that only one possible trajectory exists and thus there is no interference that could lead to colour. The effect of the refractive index contrast can be seen by adjusting n_2 (Fig. 4e). The sharp changes in colour as n_2 decreases correspond to where TIR begins to occur for another trajectory. These transitions are probably smoother than shown here, as we have not included light that is reflected with high amplitude but below the critical angle. These results suggest that it should be possible to design specific, desired structural colour patterns and fabricate the required surface to generate the predicted iridescence.

A unique aspect of the iridescent biphasic oil droplets is that they can be switched between the Janus and double emulsion morphologies by tuning the balance of interfacial tensions[22]. This morphological change allows us to manipulate the curvature of the oil–oil interface where the TIR occurs, which should, in turn, influence the reflected colour. We varied the droplet morphology between Janus and double emulsion configurations by adjusting surfactant concentrations in the water and observed that the only droplet shapes that reflect light when illuminated from above are those having a partially open and concave curvature between the two oils (for example, droplets ii to v in Fig. 5a). This is consistent with predictions, because only the partially open concave interfaces that transition from high to low refractive index can support multiple paths of TIR leading to interference. Also consistent with the model is the observation that the iridescence produced is exquisitely sensitive to slight changes in the curvature and opening angle of the oil–oil interface where TIR occurs. By introducing a light-responsive azobenzene surfactant, (4-butylphenyl)-2-(4-trimethylammonium-propoxyphenyl) diazene[22,23], we were able to use ultraviolet and blue light to photo-pattern the droplet morphologies and create reflective coloured images (Fig. 5b). Such responsive, tunable droplet colours could be of interest for sensors or displays.

We have described a design principle by which to create structural colouration via interference occurring when light undergoes multiple total internal reflections at microscale interfaces. Although this phenomenon has not been previously studied, we find it to be commonplace, as it is observed even in simple microscale droplets on transparent surfaces. Key requirements to generate this effect are: (1) an interfacial refractive index contrast that supports total internal reflection, and (2) a microscale geometry that supports multiple trajectories for total internal reflection of light for specific directions of light incidence and observation. We expect this colour effect to persist until the optical path length difference of various light trajectories along the interface exceeds the coherence length of the incident light. We have presented a detailed analytical model with predictive capabilities that are verified by close matching of experimentally determined and modelled angular colour distributions. Our model allows us to explain the colour variations observed for variables such as radius of curvature, contact angle, refractive index contrast and incident light angle. We have leveraged this optical effect to create structural colouration within a wide range of materials and geometries including sessile droplets, biphasic droplets, solid particles and polymeric microstructures with both curved and flat sides. These design principles will be of interest and use to scientists and engineers from a wide variety of fields who seek to modulate the colour and reflective optical properties of materials.

Online content

Any methods, additional references, Nature Research reporting summaries, source data, statements of data availability and associated accession codes are available at https://doi.org/10.1038/s41586-019-0946-4.

1. Dirac, P. A. M. The quantum theory of the emission and absorption of radiation. *Proc. R. Soc. A* **114**, 243–265 (1927).
2. Kuhn, H. A quantum-mechanical theory of light absorption of organic dyes and similar compounds. *J. Chem. Phys.* **17**, 1198–1212 (1949).
3. Southall, J. P. C. *Mirrors, Prisms And Lenses: A Text-Book Of Geometrical Optics* (The Macmillan Company, 1918).
4. Ghiradella, H. Light and color on the wing: structural colors in butterflies and moths. *Appl. Opt.* **30**, 3492–3500 (1991).
5. Tadepalli, S., Slocik, J. M., Gupta, M. K., Naik, R. R. & Singamaneni, S. Bio-optics and bio-inspired optical materials. *Chem. Rev.* **117**, 12705–12763 (2017).
6. Zhao, Y., Xie, Z., Gu, H., Zhu, C. & Gu, Z. Bio-inspired variable structural color materials. *Chem. Soc. Rev.* **41**, 3297–3317 (2012).
7. Land, M. F. The physics and biology of animal reflectors. *Prog. Biophys. Mol. Biol.* **24**, 75–106 (1972).
8. Kinoshita, S. & Yoshioka, S. Structural colors in nature: the role of regularity and irregularity in the structure. *ChemPhysChem* **6**, 1442–1459 (2005).
9. Vignolini, S. et al. Pointillist structural color in *Pollia* fruit. *Proc. Natl Acad. Sci. USA* **109**, 15712–15715 (2012).
10. Fernandes, S. N. et al. Structural color and iridescence in transparent sheared cellulosic films. *Macromol. Chem. Phys.* **214**, 25–32 (2013).
11. Whitney, H. M. et al. Floral iridescence, produced by diffractive optics, acts as a cue for animal pollinators. *Science* **323**, 130–133 (2009).
12. Kinoshita, S., Yoshioka, S. & Miyazaki, J. Physics of structural colors. *Rep. Prog. Phys.* **71**, 076401 (2008).
13. Merritt, E. A spectrophotometric study of certain cases of structural color. *J. Opt. Soc. Am.* **11**, 93–98 (1925).
14. Loewen, E. G. & Popov, E. *Diffraction Gratings and Applications* (CRC Press, New York, 1997).
15. Macleod, H. A. *Thin-film Optical Filters* (CRC Press, Boca Raton, 2010).
16. Hutley, M. C. Interference (holographic) diffraction gratings. *J. Phys. Educ.* **9**, 513–520 (1976).
17. Yablonovitch, E. Photonic crystals. *J. Mod. Opt.* **41**, 173–194 (1994).
18. Hulst, H. C. *Light Scattering by Small Particles* (Courier Corporation, Mineola, 1981).
19. Nussenzveig, H. M. High-frequency scattering by a transparent sphere. II. Theory of the rainbow and the glory. *J. Math. Phys.* **10**, 125–176 (1969).
20. Born, M. & Wolf, E. *Principles of Optics: Electromagnetic Theory of Propagation, Interference and Diffraction of Light* (Pergamon Press, London, 1980).
21. Wriedt, T. A review of elastic light scattering theories. *Part. Part. Syst. Charact.* **15**, 67–74 (1998).
22. Zarzar, L. D. et al. Dynamically reconfigurable complex emulsions via tunable interfacial tensions. *Nature* **518**, 520–524 (2015).
23. Chevallier, E. et al. Pumping-out photo-surfactants from an air–water interface using light. *Soft Matter* **7**, 7866–7874 (2011).

METHODS

Chemicals. All chemicals were used as received. Capstone FS-30 (Dupont); perfluorohexane(s) (98%) and 1H,1H,2H,2H-perfluorodecyl acrylate (97%) (Synquest Laboratories); Triton X-100 (Alfa Aesar); heptane (>99%) (MilliporeSigma); Sartomer CN4002 fluorinated oligomer (Arkema); 2-hydroxy-2-methyl-1-phenyl-propan-1-one (97%) (Ark Pharm Inc.); Sylgard 184 polydimethylsiloxane (PDMS) (Dow Corning); Norland Optical Adhesive 61 (Norland); Pluronic F-127 (bioreagent grade), sodium dodecyl sulfate (98%) and trimethylolpropane ethoxylate triacrylate (number average molar mass $M_n \approx 428$ g mol^{-1}) (Sigma-Aldrich). The light-responsive azobenzene surfactant, (4-butylphenyl)-2-(4-trimethylammoni-umpropoxyphenyl) diazene, was synthesized as described in ref. [23].

Refractive index measurement of droplet oils. Heptane and perfluorohexane were mixed in a 1:1 volume ratio at ambient temperature and allowed to phase-separate, simulating the fluid conditions inside the biphasic droplets. The two phase-separated oil layers were then extracted and their refractive indices were measured using a J457FC refractometer (Rudolph Research Analytical). The refractive indices of the oils differ from the pure chemicals owing to a degree of mutual solubility.

Fabrication of droplets. Fabrication of monodisperse emulsions was accomplished using a flow focusing four-channel glass hydrophilic microfluidic chip with a 100-μm channel depth (Dolomite). Each inlet microchannel was connected to a reservoir of the desired liquids. The inlets for the inner phase fluids (for example, heptane and perfluorohexane) were connected to the reservoirs with inner diameter 0.0025 inch, outer diameter 1/16 inch polyether ether ketone (PEEK) tubing 26 inches in length, and the outer phase aqueous surfactant solution was connected to the reservoirs with inner diameter 0.005 inch, outer diameter 1/16 inch PEEK tubing 26 inches in length. The flow rate of each liquid was controlled by a Fluigent MFCS-EZ pressure controller, thus providing the ability to vary the size of the drops and the volume ratios of the liquids in each drop. Typical pressures for the inner phase fluids ranged from 1,000 mbar to 7,000 mbar and pressures for the outer phase fluids ranged from 200 mbar to 3,000 mbar. Varying ratios of Capstone FS-30 and Triton X-100 surfactants were used to tune the droplet shape via mechanisms described in detail in ref. [22]. Although many concentrations and ratios of surfactants could be used, as an example we often used aqueous solutions of 1.5 wt% Capstone FS-30 and 0.05 wt% Triton X-100 to stabilize a morphology of droplet which produced the iridescence. Additional Capstone FS-30 and Triton X-100 could be added to tune the droplet shape as desired.

Fabrication of particles. Biphasic droplet emulsions were created through the use of a 4-channel microfluidics apparatus as described in the Methods section 'Fabrication of droplets'. To make particles, monomers were used as the fluids for subsequent polymerization into particles. The hydrocarbon monomer was trimethylolpropane ethoxylate triacrylate with 5 vol% photoinitiator, 2-hydroxy-2-methyl-1-phenylpropan-1-one. The fluorinated monomer was Sartomer CN4002 fluorinated oligomer mixed with 1H,1H,2H,2H-perfluorodecyl acrylate in a 3:1 volume ratio. 1 wt% Pluronic F-127 in water was used as the continuous phase. PEEK tubing of length 2 feet with inner diameter 0.005 inch and pressures of 500 mbar were used for all four inlet flows. Once the droplets were fabricated, 1 wt% sodium dodecyl sulfate in water was added to the droplet solution until the droplets exhibited a Janus shape that reflected light. Droplets were then polymerized into solid particles by curing under an OmniCure ultraviolet lamp (mercury bulb, 17 W cm^{-2}) for 30 s.

Microscopic imaging for determining droplet shape. The droplets were imaged using a Nikon Eclipse Ti-U inverted microscope. The droplets naturally orient with the denser fluorocarbon side downward, so to image the droplet profile, the emulsions were shaken in order to induce the droplets to roll onto their sides and then the image was captured using a <1-ms exposure with an Image Source DFK 23UX249 colour camera. To image droplets in reflection, an upright microscope with a QImaging Micropublisher 3.3 RTV colour camera was used.

Macroscopic imaging of droplet colour. A monolayer of the emulsion droplets was placed in a Petri dish with aqueous surfactant solution. The bottom of the dish was painted with black acrylic paint. For large area illumination, an Amscope LED 50 W light with a collimating lens was used to illuminate the sample. For selected area illumination, a Thorlabs LED light (MWWHF2, 4,000 K, 16.3 mW) equipped with a 200-μm-diameter fibre optic cable and collimating lens (CFC-2X-A) was used. The translucent dome used for capturing the iridescent colour pattern was created by cutting a 40-mm-diameter ping-pong ball in half with a razor blade and drilling a 3-mm-diameter hole in the side with a Dremel Model 220. The ping-pong ball dome screen was then placed on the 35-mm Petri dish lid containing the emulsion and collimated light from the LED was passed through the hole into the centre of the dish. All macroscale photographs were taken using a Canon EOS Rebel T6 DSLR camera mounted on an optical table and positioned at specific angles, as indicated in the main text.

Reflection from sessile water drops and contact angle. The advancing contact angle of water on a polystyrene Petri dish was measured using a goniometer (ramé-hart). Sessile water drops were imaged in reflection using a Nikon Eclipse Ti-U inverted microscope (for microscopic imaging) or with a Canon EOS Rebel T6 DSLR camera (for macroscopic photographs). The water drops were created by placing warm water in a dish under the room temperature Petri dish substrate and allowing water to condense. The macroscale patterned reflectance image of the elephant was created using selected area ultraviolet-ozone treatment to increase the hydrophilicity of the polystyrene surface. A laser cutter was used to cut an elephant shape out of paper which was placed over the hydrophobic surface of a polystyrene Petri dish to use as a mask during ultraviolet-ozone treatment. Unexposed areas of the polystyrene remained hydrophobic, while ultraviolet-ozone treated areas were hydrophilic (low contact angle) and no longer supported total internal reflection and hence had no iridescent colour.

Multiphoton lithography fabrication. Arrays of solid domes, horizontal cylindrical segments, and polygons were created using the Photonic Professional GT Nanoscribe. This equipment allows the user to 3D-print structures using multiphoton near-infrared direct laser writing. Structures were printed onto fused silica glass slides with a 60× objective with the resist IP-Dip 65 ($n = 1.54$) or IPS ($n = 1.51$) using a 100-nm or 200-nm step size. The domes were computationally rendered with 3ds Max software (https://www.autodesk.com/products/3ds-max/overview) and the cylinders and polygons were rendered with AutoCAD (https://www.autodesk.com/products/autocad/overview). Both renderings were converted into a DeScribe file format to import into the Nanoscribe. Uncured resist was washed away with AZEBR solvent (MicroChemicals) for 20 min and isopropanol for 2 min.

Replication of polymer structures. Dow Corning Sylgard 184 PDMS was used to create a replica from the structures printed with the Nanoscribe. The PDMS base and hardener were mixed in a 10:1 mass ratio, poured over the polymer sample, and cured in an oven at 70 °C for at least two hours. The cured PDMS was peeled off the structures to yield an array of wells. The PDMS mould could then be used to replicate the structures into different refractive index polymers, such as Norland Optical Adhesive (NOA) 61 ($n = 1.56$). After allowing the polymer to fill the PDMS wells, the sample was backed with glass, and the resin was cured using an ultraviolet lamp (17 W cm^{-2} for 20 s). The NOA 61 was then peeled out of the PDMS mould to yield an array of replicated structures.

Effect of refractive index contrast. Domes fabricated in NOA 61 ($n = 1.56$) on a glass substrate could be placed in various solvents to observe the effects on refractive index contrast on the colour. In Supplementary Video 3, the domes were imaged in reflection using a Nikon Ti-U Eclipse and Image Source DFK 23UX249 colour camera. NIS-Elements software was used to record a video of the reflected colours as methanol evaporated off the surface.

Implementation of the theoretical optical model. The model presented in the main text was implemented in MATLAB (see Methods section 'Code availability'). In the two-dimensional case, the parameters for the radius of curvature of the droplet-internal interface R, the refractive indices n_1 and n_2, the contact angle η, and the light incidence angle θ_{in} were fixed and the following sum was computed for each value of observation angle θ_{out} and light wavelength λ_0:

$$I = \left| \sum_{m_{+\min}}^{m_{+\max}} \sqrt{\frac{\cos(\alpha_{m+})}{m}} r_+^m \exp\left(4i\pi n_1 \frac{R}{\lambda_0} m \cos(\alpha_{m+})\right) \right|^2$$
$$+ \left| \sum_{m_{-\min}}^{m_{-\max}} \sqrt{\frac{\cos(\alpha_{m-})}{m}} r_-^m \exp\left(4i\pi n_1 \frac{R}{\lambda_0} m \cos(\alpha_{m-})\right) \right|^2$$

with

$$\alpha_{m\pm} = \frac{\pi}{2} - \frac{\pi \pm (\theta_{out} - \theta_{in})}{2m}, \quad m_{\pm \min} = \frac{\pi \pm (\theta_{out} - \theta_{in})}{\left(\pi - 2\sin^{-1}\left(\frac{n_2}{n_1}\right)\right)}$$

and

$$m_{\pm \max} = \frac{\pi \pm (\theta_{out} - \theta_{in})}{(\pi - 2\alpha_{\pm \max})}$$

where

$$\alpha_{\pm \max} = \min\left(\frac{\pi}{2} - \left|\frac{\pi}{2} - (\eta \pm \theta_{in})\right|, \frac{\pi}{2} - \left|\frac{\pi}{2} - (\eta \mp \theta_{out})\right|\right)$$

(see Supplementary Discussion for detailed derivations). r_+ and r_- are the Fresnel coefficients, which depend on the refractive index contrast n_1/n_2, the light polarization, and α_{m+} and α_{m-} respectively. The two sum-squared terms represent the two different families of light trajectories for light incident and reflected at the same angles on opposing sides of the concave optical interface.

In the model, output spectra were averaged for input illumination angles lying in a cone from $-5°$ to $+5°$ to approximate the small divergence of the light source used in the experiments, and the lamp's spectrum was used for input spectral intensities. The calculated intensity spectrum for each value of θ_{out} can then be converted to CIE xyz colour coordinates using the colour-matching functions[24,25]. The CIE coordinates were then converted to sRGB (standard Red Green Blue)[26] in order to be displayed.

For three dimensions, the same sum was used but with

$$\alpha_{m\pm} = \frac{\pi}{2} - \frac{\pi \pm (\beta_{out} - \beta_{in})}{2m}, \quad m_{\pm min} = \frac{\pi \pm (\beta_{out} - \beta_{in})}{\left(\pi - 2\sin^{-1}\left(\frac{n_2}{n_1}\right)\right)}$$

and

$$m_{max} = \frac{\pi \pm (\beta_{out} - \beta_{in})}{(\pi - 2\alpha_{max})}$$

where $\alpha_{max} = \min\left(\frac{\pi}{2} - |\frac{\pi}{2} - (\eta_{eff} + \beta_{in})|, \frac{\pi}{2} - |\frac{\pi}{2} - (\eta_{eff} - \beta_{out})|\right)$. β_{in}, β_{out} and η_{eff} are the effective angles in the plane of incidence as shown in Fig. 4a. They are related to the global angles by:

$$\cos(\beta_{in}) = B\cos\theta_{in}$$

$$\cos(\beta_{out}) = -B\cos(\theta_{out})$$

$$\cos(\eta_{eff}) = B\cos(\eta)$$

with

$$B = \frac{|\sin(\psi)|}{\sqrt{(\sin^2(\psi) - \sin^2(\theta_{in})\sin^2(\theta_{out})\sin^2(\phi_{out}))}}$$

Here, ψ is the angle between the incoming and outgoing ray of light:

$$\cos(\psi) = \sin(\theta_{out})\sin(\theta_{in})\cos(\phi_{out}) + \cos(\theta_{in})\cos(\theta_{out})$$

To visualize the data in a manner similar to the ping-pong ball projections, theoretical angular colour distribution maps were created from the calculated intensities $I(\lambda, \theta_{out}, \phi_{out})$ and the corresponding sRGB colours. The (x, y) coordinates of the colour distribution image (measured from the centre) relate to the direction of observation via the equations $x = k\sin(\theta_{out})\cos(\phi_{out})$ and $y = k\sin(\theta_{out})\sin(\phi_{out})$ where k is an arbitrary scaling factor to set the image size.

Code availability. The MATLAB code used to implement the model is available for download from https://github.com/snnagel/Structural-Color-by-Cascading-TIR.

Data availability
All relevant data generated or analysed for this study are included in this published article (and its Supplementary Information files).

24. *CIE 015:2004: Colorimetry Technical Report* 3rd edn http://cie.mogi.bme.hu/cie_arch/kee/div1/tc148.pdf (Commission Internationale de l'Éclairage, 2004).
25. Gupte, V. C. in *Colour Measurement: Principles, Advances and Industrial Applications* 70–86 (Woodhead, Philadelphia, 2010).
26. Burger, W. & Burge, M. J. in *Digital Image Processing* 341–365 (Springer, London, 2016).
27. Polyanskiy, M. N. *Refractive Index Database* https://refractiveindex.info/ (2018).
28. Stiles, V. E. & Cady, G. H. Physical properties of perfluoro-*n*-hexane and perfluoro-2-methylpentane. *J. Am. Chem. Soc.* **74**, 3771–3773 (1952).
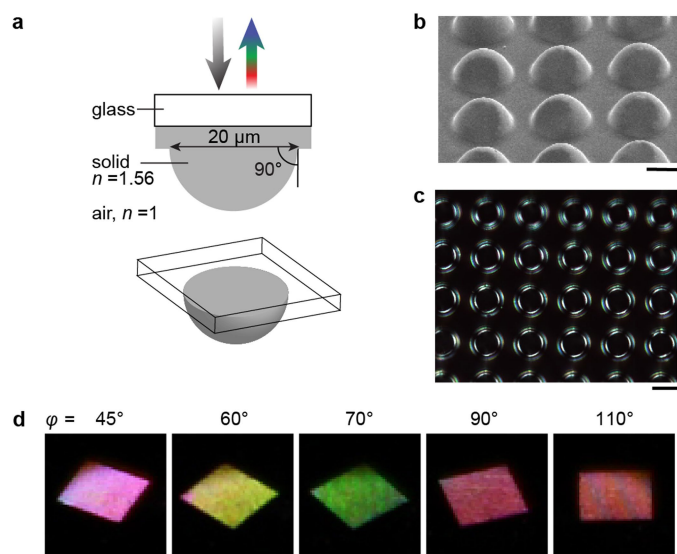
Extended Data Fig. 1 | Transparent, polymeric hemispheres printed with multiphoton lithography display iridescence. a, Schematic of the geometry of the hemispheres. **b**, Scanning electron micrograph of the polymeric hemispheres. Scale bar, 10 μm. **c**, Reflection optical micrograph of the transparent hemispheres. Scale bar, 20 μm. **d**, Macroscopic Canon EOS Rebel T6 DSLR photographs of the hemisphere array as viewed by rotating the camera around the sample under a constant illumination angle. Scale bar, 1 mm.
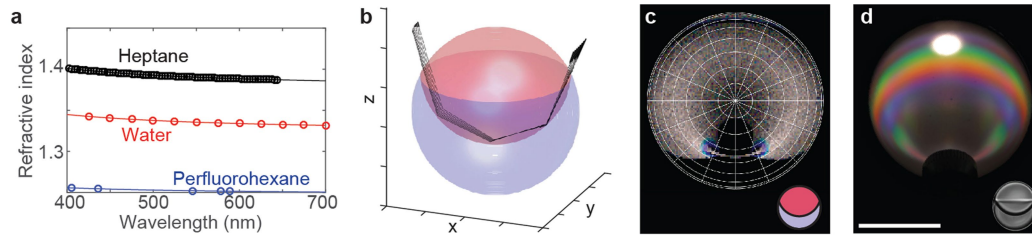
Extended Data Fig. 2 | Material dispersion in biphasic droplets does not fully account for the colour separation. a, Refractive index as a function of wavelength for each of the droplet materials. Water and heptane are both more dispersive than perfluorohexane[27,28]. **b**, Ray-tracing diagram through the droplet, where the red phase is heptane and the grey phase is perfluorohexane. Ray trajectories were determined for a large number of rays, with different refractive index values for each wavelength. Outgoing rays were binned according to angle and wavelength and for each (θ, φ) pixel the spectrum was converted to colour, yielding **c**, the colour separation diagram due to material dispersion. Binning was only necessary for the ray-tracer data taking into account the curved upper interface of the droplets. Nothing is binned in the analytical interference model that was used to explain the observed effects. The only colour separation is a small amount of blue, where total internal reflection just starts (because the critical angle for blue light is smaller than that of red light). **d**, Experimental iridescent colour distribution from a similar droplet geometry for comparison. Scale bar, 20 mm.
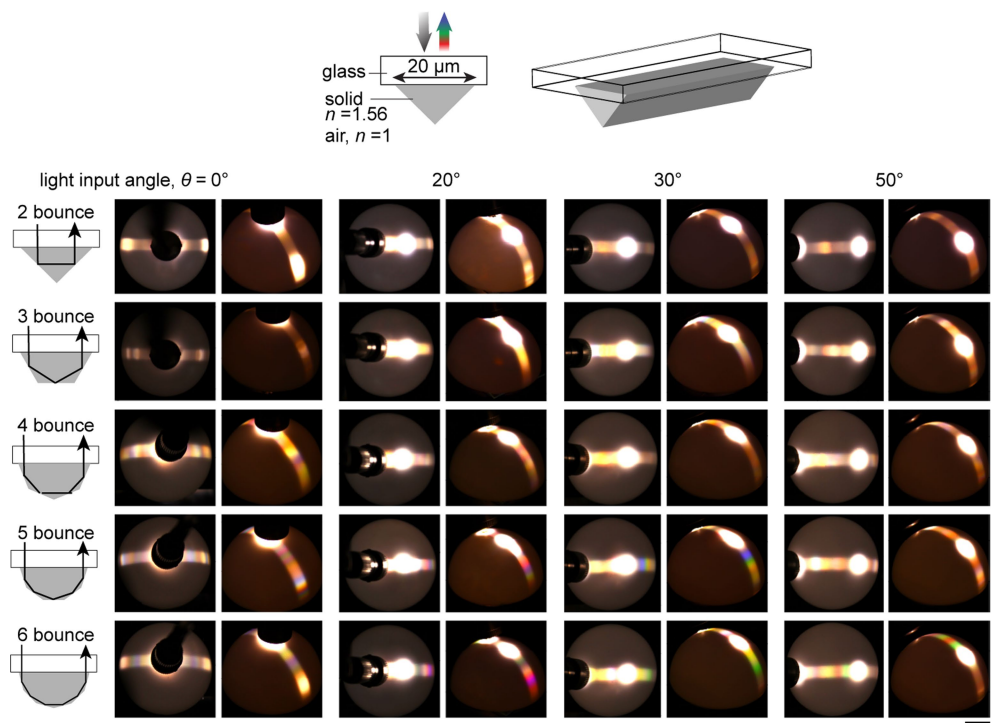
Extended Data Fig. 3 | Flat-sided polygonal segments printed with multiphoton lithography display iridescence. The number of sides in the polygon serves to limit the maximum possible number of total internal reflections (diagram at left) that light can undergo for a given illumination angle. Shown are Canon EOS Rebel T6 DSLR photographs of the reflected colour distributions produced by the method described in Fig. 2a. The light input direction is provided as θ and the dome was photographed from two viewing angles. Each polygon had a base width of 20 μm. Scale bar, 1 cm.
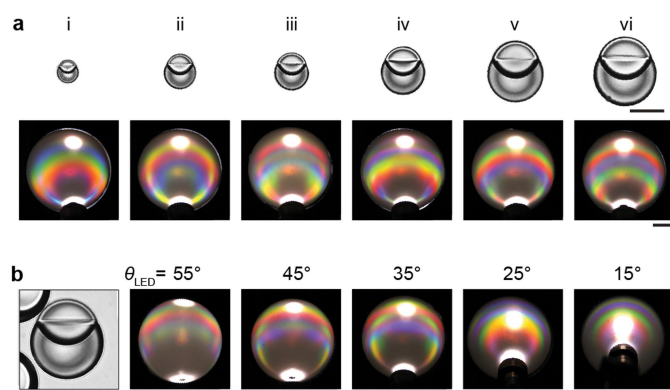
Extended Data Fig. 4 | Effect of droplet size and illumination angle on the reflected colour distribution from biphasic droplets. a, The iridescence of monodisperse heptane–perfluorohexane droplets with varying diameter but consistent morphology was investigated. The top row shows optical micrographs of a droplet from each sample. Scale bar, 100 μm. The bottom row shows photographs of the angular colour distribution pattern as viewed from $\theta = 0°$ with an illumination angle of $\theta = 35°$. **b,** Optical micrograph (far left) of an example biphasic droplet containing heptane and perfluorohexane (scale bar, 50 μm) and photographs of the angular colour distributions as viewed from $\theta = 0°$ when the illumination angle is altered, as shown (scale bar, 1 cm).